International Journal on Engineering Technology and Infrastructure Development (InJET-InDev)
www.lec.edu.np/journal
Volume 2, Issue no. 2, Page 212-225
Received Date: 12/5/2025
Revised Date: 5/13/2026
Accepted Date: 5/22/2026
ISSN: 3021-999X (Print)
https://doi.org/10.3126/injet-indev.v2i2.95727

# Numerical Analysis of Deep Basement Excavation in Soft Soils of Kathmandu Valley

Rajan Tiwari[1], Ram Chandra Tiwari[2], Aanchal Tiwari[3] *

[1]*Former student, M.Sc. In Geotechnical Engineering, Department of Civil Engineering, Pulchowk Campus, IoE, T.U., Nepal, rajant662@gmail.com*
[2]*Asst. Prof., Department of Civil Engineering, Pulchowk Campus, IoE, T.U., Nepal, rct2075ce_rctiwari@pcampus.edu.np*
[3]*Asst. Prof., Department of Civil Engineering, Cosmos College of Management and Technology, P.U., Nepal & Former Student, M.Sc. In Transportation Engineering, Department of Civil Engineering, Pulchowk Campus, IoE, T.U., Nepal, 079mstre001.aanchal@pcampus.edu.np*

**Abstract**

This study investigates the soil–structure interaction behavior of a deep excavation support system at the Ramshahpath site using three-dimensional finite element modelling. The primary objective is to evaluate ground deformation, pile response, and structural performance under varying pile diameters, surcharge positions, construction stages, and constitutive soil models. The subsurface soil at the site predominantly consists of fine-grained clayey silt with low to intermediate plasticity. Numerical simulations were carried out using PLAXIS 3D, employing both the Mohr–Coulomb (MC) and Modified Cam Clay (MCC) constitutive models. The results indicate that pile diameter plays a significant role in controlling system stiffness and deformation, with an increase from 0.65 m to 0.90 m reducing lateral pile displacement by up to 18% and surface settlement by more than 30%. The structural response is also strongly influenced by surcharge load position and construction sequence; surcharge applied at the ground surface induces cantilever-type deformation, while deeper loading reduces displacement and promotes a more uniform stress distribution within the soil mass. A comparative analysis of constitutive models shows that the MC model tends to overestimate deformations, predicting lateral wall movements up to 67 mm, whereas the MCC model provides significantly lower and more realistic responses (approximately 4–7 mm), making it more suitable for soft clay conditions. The numerical results were validated using Matlock p–y empirical relationships, published literature, and relevant empirical methods, showing acceptable agreement in deformation trends and confirming the reliability of the finite element modelling approach. Overall, the study emphasizes that increased pile stiffness, appropriate positioning of surcharge loads, and the use of advanced constitutive models are essential for effectively controlling excavation-induced deformation and improving the reliability of predictions in soft soil environments.

*Keywords*: Deep excavation, Soil–structure interaction (SSI), Finite Element Method (FEM), Modified Cam Clay model (MCC), Mohr–Coulomb model (MC)

## 1. Introduction

Deep excavations significantly modify in-situ stress conditions, causing stress redistribution, ground settlement, and lateral soil movement. These effects may reduce the bearing capacity of nearby foundations and increase earth pressures on support systems. The arching effect, governed by relative stiffness between soil and structure, controls load transfer, while excavation also alters groundwater flow and pore pressure conditions. To mitigate these risks, staged excavation with appropriate shoring (for depths >1.5 m) and impermeable retaining systems such as piling and jacketing are commonly adopted. Early empirical frameworks by Peck (1969) classified excavation performance into three categories based on soil type and stability number, highlighting that soft clays exhibit significantly higher lateral movements than sands, especially when strut installation is delayed. Later, Mana and Clough (1981) demonstrated that excavation-induced movements increase with decreasing factor of safety (FOS) against basal heave. Clough and O'Rourke (1990) further established settlement influence zones (≈$2H_e$ for sands and $3H_e$ for clays) and introduced system stiffness as a governing parameter:

$$K_s = \frac{EI}{\gamma_w h_{av}^4} \qquad \text{(Equation 1)}$$



*Corresponding Authors

Where $EI$ is the flexural rigidity of retaining system, $\gamma_w$ is the unit weight of water, and $h$ is the excavation depth. The stability against basal heave is commonly evaluated using Terzaghi's formulation for undrained clay:

$$FOS = \frac{C_u N_c}{\gamma D} \qquad \text{(Equation 2)}$$

Where $C_u$ is undrained shear strength, $\gamma$ is total (bulk/moist) unit weight of soil, $D$ is excavation depth, and $N_c \approx 5.14$ (Terzaghi, 1943; Peck, 1969). This study aims to numerically evaluate excavation support performance in the soft sediments of the Kathmandu Valley, focusing on soil–structure interaction, ground deformation, and the influence of system stiffness and key geotechnical parameters using advanced constitutive soil models. Figure 1 shows the study area located at Ramshahpath, Kathmandu, while Figure 2 illustrates the behavior of an excavation support system as reported by Sharma et al. (2019).

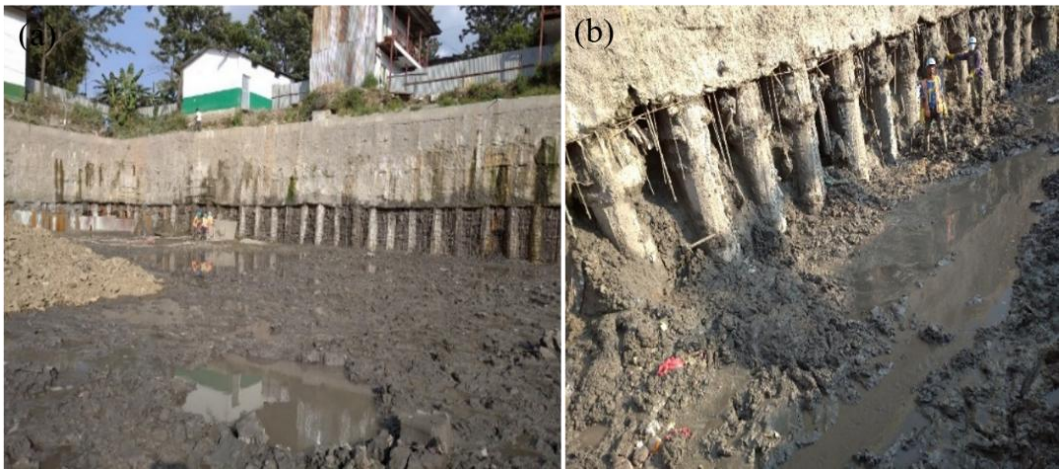


Figure 1. Study area (Ramshahpath, Kathmandu): (a) piling and jacketing construction works, (b) preparation of structural jacketing

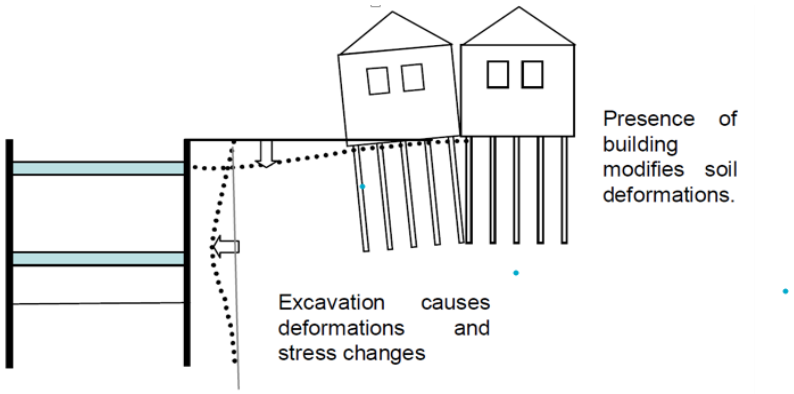


Figure 2. Behavior of Excavation Support System (Sharma et al., 2019)

## 2. Methodology

Figure 3 presents the flow chart of the methodology adopted in this study, outlining the sequential steps followed from data collection and soil characterization through numerical modeling, analysis of excavation support systems, and evaluation of results. The methodology of this study begins with a comprehensive review of relevant codes and literature to establish a strong theoretical foundation. This is followed by the selection of a suitable site for deep excavation analysis in the Kathmandu Valley. A detailed site visit is then conducted, including soil sampling and data collection (Figure 4). The collected samples are subjected to laboratory testing to determine key parameters such as compression index (Cc), swelling index (Cs), coefficient of volume compressibility (Mv), modulus of elasticity (E), and void ratio (e). Based on these results, material properties and geometric conditions are characterized for analysis. Subsequently, a three-dimensional numerical model of the site is developed using PLAXIS 3D, and deformation analysis of the soil and retaining structures is performed. The results are then compared using two constitutive models, namely the Mohr–Coulomb model and the Modified Cam Clay model,

to evaluate their performance. Finally, the numerical results are verified against available literature and empirical methods to ensure reliability and accuracy.

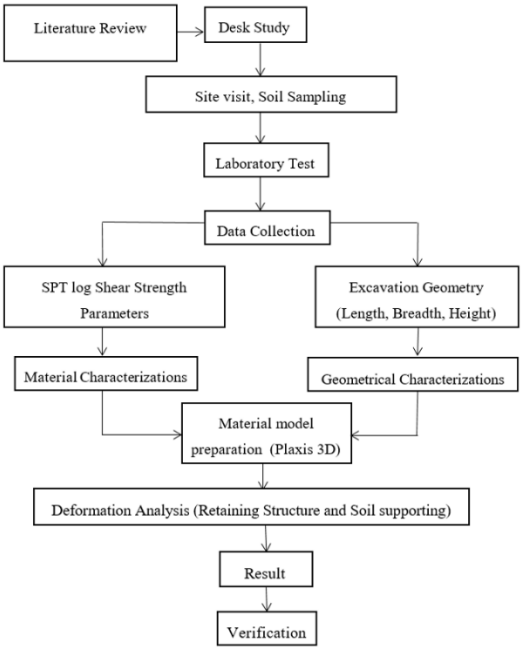


Figure 3. Flow Chart of Methodology


Figure 4. Soil sampling for consolidation test: (a) field sampling location, (b) collection of undisturbed soil samples

### *2.1 Material Model*

Laboratory testing was conducted to determine the engineering properties of the soil, including index properties such as grain size distribution, liquid limit ($LL$), plastic limit ($PL$), and specific gravity. In addition, consolidation tests were performed to evaluate the compressibility characteristics of the soil, where the consolidation process represents the gradual expulsion of pore water from the soil mass under applied loading, resulting in volume reduction and settlement over time. Laboratory Testing and Consolidation (Equations 3-6): These are standard geotechnical principles derived from Terzaghi (1943). Empirical $C_c$ Correlations (Equations 7-8): These specific constants (0.009 and 0.007) were established by Skempton (1944) and later popularized by Terzaghi and Peck (1967). The theoretical foundation for this Modified Cam Clay model is credited to Roscoe and Burland (1968). For numerical verification, Brinkgreve et al. (2023) is used for the PLAXIS material models Manual. Table 1 presents the results of laboratory consolidation tests conducted on the soil samples.

$$\Delta H = H\left(\frac{\Delta e}{1+e_0}\right) \qquad \text{(Equation 3)}$$

Where $e_0$ = initial void ratio = $\omega_{nat} \times G_s$, $\omega_{nat}$ = natural water content

$$a_v = (-)\frac{\Delta e}{\Delta \acute{\sigma}} \quad \text{(Equation 4)}$$

$$C_c = \frac{\Delta e}{log\left(\frac{\acute{\sigma}_0 + \Delta \acute{\sigma}}{\acute{\sigma}_0}\right)} \quad \text{(Equation 5)}$$

$$m_v = \frac{a_v}{1+e_0} \quad \text{(Equation 6)}$$

Where $C_c$ (Compression Index) is the slope of the virgin compression line in the $e - log\sigma$ consolidation curve. $C_s$ is the slope of unloading portion of curve curve.

$$C_c = 0.009 \times (LL - 10\%), \text{ for natural soil} \quad \text{(Equation 7)}$$

$$C_c = 0.007 \times (LL - 10\%), \text{ for re-moulded soil} \quad \text{(Equation 8)}$$

Equations (3-6) are based on laboratory consolidation test results, while Equations (7, 8) are empirical correlations used only for comparison and verification of the compression index obtained from tests.

Table 1. Laboratory test of consolidation Results of Soil

| **Parameters** | **Value** |
|---|---|
| $C_c$ | 0.16 |
| $C_s$ | 0.02 |

The Mohr–Coulomb model is one of the most commonly used constitutive models in geotechnical design due to its simplicity and the limited number of input parameters required, making it practical for preliminary analysis and routine engineering applications. In contrast, the Modified Cam Clay model is an advanced elasto-plastic model specifically developed to simulate the behavior of soft clays more realistically, particularly under loading and consolidation conditions. Although the theoretical framework of the Modified Cam Clay model is more complex, the required soil parameters are relatively straightforward and many can be reasonably estimated using established correlations based on Atterberg's limits. Table 2 summarizes the corresponding input parameters for both constitutive models, Mohr–Coulomb (MC) and Modified Cam-Clay (MCC) models at the Ramshahpath excavation site.

Table 2. Input parameters of drained soil for the Mohr–Coulomb (MC) and Modified Cam-Clay (MCC) models at the Ramshahpath site

| **S. No.** | **Parameters** | **Unit** | **Depth (m)** | | |
|---|---|---|---|---|---|
| | | | **0-3** | **3-6** | **6-30** |
| 1 | Unit Weight, $\gamma$ | kN/m$^3$ | 17.00 | 16.90 | 16.50 |
| 2 | Effective cohesion, $C$ | kN/m$^2$ | 4.72 | 4.72 | 4.72 |
| 3 | Effective friction angle, $\emptyset$ | [ ° ] | 32.7 | 33 | 31 |
| 4 | Dilatancy angle, $\varphi$ | [ ° ] | 2.7 | 3 | 1 |
| 5 | Effective Young's modulus, $E$ | kN/m$^2$ | 1836 | 1923 | 1662 |
| 6 | Effective Poisson's ratio, $\mu$ | [-] | 0.3 | 0.3 | 0.31 |
| 7 | Cam-Clay compression index λ | [-] | 0.07 | 0.067 | 0.075 |
| 8 | Cam-Clay swelling index, $K$ | [-] | 0.02 | 0.09 | 0.017 |
| 9 | Initial void ratio for loading/unloading | [-] | 0.86 | 0.87 | 0.81 |
| 10 | Tangent of the critical state line, $M$ | [-] | 1.71 | 1.79 | 1.63 |
| 11 | Coefficient of lateral stress in normal consolidation derived from $M, K_0$ | [-] | 0.46 | 0.45 | 0.47 |

Table 3 presents the geometric characterization such as depth of GWT, excavation depth,$D_f$ length of excavation, width of excavation, surcharge intensity, surcharge depth, etc. of the excavation site at Ramshahpath.

Table 3. Geometric characterization of Ramshahpath excavation site

| S. No. | Parameters | Unit | Input Value |
|---|---|---|---|
| 1 | Depth of GWT | m | -1.5 |
| 2 | Excavation depth, $D_f$ | m | 8.5 |
| 3 | Length of excavation | m | 131.4 |
| 4 | Width of excavation | m | 72 |
| 5 | Surcharge Intensity | kN/m$^2$ | 30 |
| 6 | Surcharge Depth | m | -2,-2.5,-3 |

### *2.2 Numerical Model*

Figure 5 presents a comprehensive 3D finite element analysis of the excavation site, illustrating the SSI effect through a progression from initial geometry to structural performance. The Figure (a) establishes the 3D PLAXIS model geometry, defining the complex interaction between the soil stratigraphy and the support system. In the Figure (b), the deformed mesh highlights the total displacement field as the soil reacts to the combined influence of surface surcharge loading and sequential excavation, showing potential settlement zones behind the wall. Finally, the Figure (c) isolates the lateral deformation profile of the capping beam, providing a critical structural metric to ensure that horizontal deflections remain within permissible engineering limits for the safety of adjacent urban infrastructure. Boundary conditions were defined to minimize boundary effects on the numerical results. The lateral boundaries were restrained in the horizontal direction while allowing vertical movement, and the bottom boundary was fully fixed in both horizontal and vertical directions. The model domain was extended sufficiently beyond the excavation area to ensure that boundary constraints did not influence the soil–structure interaction response. A refined mesh was adopted in the vicinity of the excavation and retaining system to capture stress concentration and deformation accurately, while a relatively coarser mesh was used away from the excavation zone to optimize computational efficiency without affecting overall results.

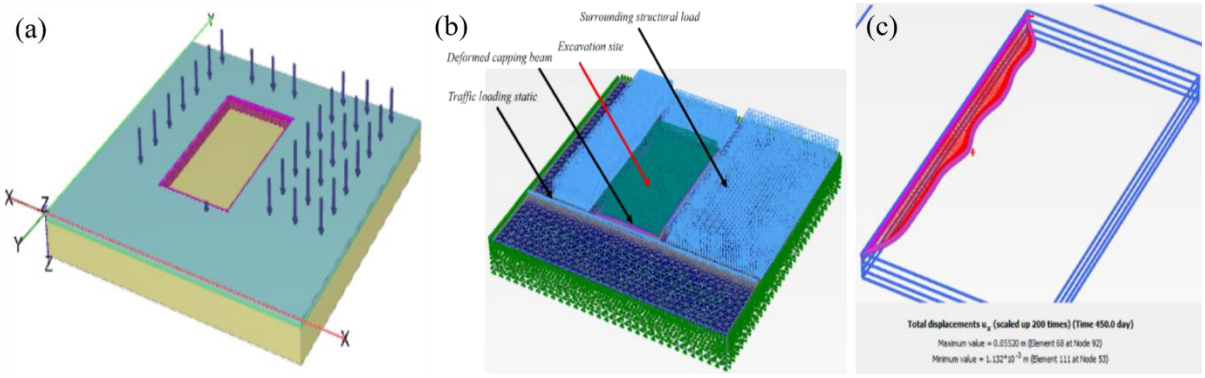


Figure 5. Ramshahapath site: (a) 3D PLAXIS model, (b) deformed mesh under surface loading and excavation, (c) lateral deformation of capping beam under surface loading and excavation

The estimation of input parameters is carried out using standard empirical relationships. The model parameters, namely the compression index ($\lambda$) and swelling index (K), are expressed as:

Model parameter, $\lambda$ and K:

$$\lambda = \frac{\mathrm{Cc}}{2.3*(1+e)} \;\&\; \mathrm{K} = \frac{\mathrm{Cs}}{2.3(1+e)} \qquad \text{(Equation 9)}$$

The pile load capacity is estimated using the undrained bearing capacity approach:

$$\mathrm{Qp} \approx \mathrm{Nc} * \mathrm{Cu} * \mathrm{Ap} = 9\mathrm{CuAp} \qquad \text{(Equation 10)}$$

$$f_{av} = \lambda(\sigma_{av} + 2\mathrm{C}_u) \qquad \text{(Equation 11)}$$

Table 4 presents the input parameters used for the case study of the Ramshahpath building site. The data include geometric dimensions of the excavation, applied surface and traffic loadings on different sides, and key structural elements such as pile length, embedment depth, pile diameter, capping beam dimensions, pile spacing, and total number of piles used in the analysis. These parameters form the basis for the numerical modelling and ensure realistic simulation of field conditions.

Table 4. Input of case study of Ramshahpath building construction site

| S. No. | Parameters | Unit | Quantity |
|---|---|---|---|
| 1 | Length of excavation | m | 131.4 |
| 2 | Width of excavation | m | 70.4 |
| 3 | Depth of excavation | m | 8.5 |
| 4 | Surface loading at North side | $kN/m^2$ | 30 |
| 5 | Surface loading at South side | $kN/m^2$ | 25 |
| 6 | Surface loading at East side | $kN/m^2$ | 25 |
| 7 | Traffic loading at West side | $kN/m^2$ | 5 |
| 8 | Length of pile | m | 17 |
| 9 | Length of embedment | m | 8.5 |
| 10 | Diameter of Pile | m | 0.8 |
| 11 | Capping Beam Depth | m | 0.65 |
| 12 | Capping Beam Width | m | 0.8 |
| 13 | Spacing of pile | m | 0.8 |
| 14 | No of pile | No | 226 |

## 3. Results and Discussions

The effect of surcharge load position on horizontal displacement ($u_x$) at the excavation site along the shorter side of the excavation is presented in Figure 6 and summarized in Table 5. When the surcharge load is applied at the ground surface, the maximum lateral displacement reaches 12.5 mm at a depth of approximately -8.5 m, with a toe displacement of 8.5 mm at -18 m depth. In contrast, when the surcharge load is applied 2.5 m below the excavation level, the peak displacement significantly reduces to 5.2 mm at about -8.0 m depth, and the corresponding toe displacement decreases to 4.2 mm. This comparison clearly indicates that relocating the surcharge load closer to the excavation base effectively reduces lateral soil movement and improves overall stability of the excavation system. The results presented in Figures 6-9 and Tables 5-8 correspond to analyses performed using the Mohr-Coulomb (MC) constitutive model unless otherwise specified.

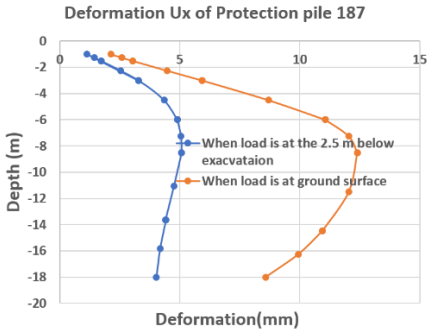


Figure 6. Ux effect of position of surcharge load, shorter side of excavation

Table 5. Ux effect of position of surcharge load, shorter side of excavation

| Loading Condition | Peak Displacement | Depth of Peak | Toe Displacement (-18m) |
|---|---|---|---|
| At Ground Surface | 12.5 mm | -8.5 m | 8.5 mm |
| 2.5m Below Excavation | 5.2 mm | -8.0 m | 4.2 mm |

The effect of surcharge load position on vertical displacement ($u_y$) along the shorter side of the excavation is illustrated in Figure 7 and summarized in Table 6. When the surcharge load is applied at the ground surface, the maximum vertical displacement reaches 13 mm at a depth of approximately -8.5 m, with a toe displacement of 9.5 mm at -18 m depth. In contrast, when the surcharge load is applied 2.5 m below the excavation level, the peak displacement reduces significantly to 5.5 mm at the same depth (-8.5 m), while the toe displacement decreases to 4.0 mm. This demonstrates that shifting the surcharge load closer to the excavation level effectively minimizes vertical deformation and enhances the stability of the excavation system.

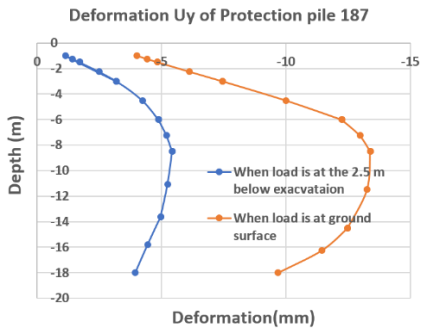


Figure 7. Uy effect of position of surcharge load, shorter side of excavation

Table 6. Uy effect of position of surcharge load, shorter side of excavation

| Loading Condition | Peak Displacement | Depth of Peak | Toe Displacement (-18m) |
|---|---|---|---|
| At Ground Surface | 13 mm | -8.5 m | 9.5 mm |
| 2.5m Below Excavation | 5.5 mm | -8.5 m | 4.0 mm |

The effect of surcharge load position on vertical ground response (uz) site along the shorter side of the excavation is presented in Figure 8 and summarized in Table 7. When the surcharge load is applied 2.5 m below the excavation level, an upward displacement (heave) of 8.0 mm is observed, indicating stress relief and upward soil movement. In contrast, when the surcharge load is applied at the ground surface, a downward displacement (settlement) of −3.0 mm occurs. This behavior highlights that the position of surcharge load not only influences the magnitude but also the direction of vertical ground movement, with subsurface loading inducing heave and surface loading resulting in settlement.

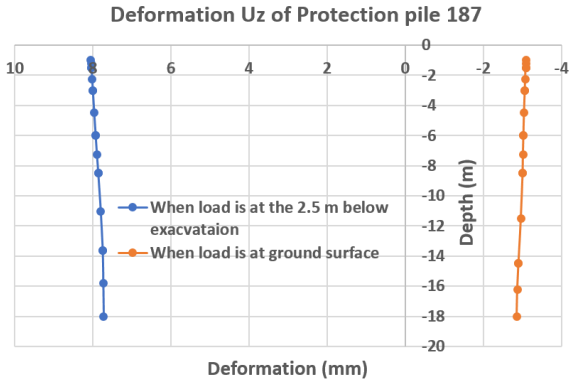


Figure 8. Uz effect of position of surcharge load, shorter side of excavation

Table 7. Uz effect of position of surcharge load, shorter side of excavation

| Loading Condition | Displacement (mm) | Type of Movement |
|---|---|---|
| 2.5 m Below Excavation | 8.0 mm | Heave (Upward) |
| At Ground Surface | -3.0 mm | Settlement (Downward) |

The effect of surcharge load position on horizontal displacement ($u_x$) along the longer side of the excavation is illustrated in Figure 9 and summarized in Table 8. When the surcharge load is applied at the ground surface, a significantly higher head displacement of 67 mm is observed, with a toe displacement of 32 mm at −18 m depth, resulting in a total deformation of 35 mm across the excavation depth. In contrast, when the surcharge load is applied 2.5 m below the excavation level, the head displacement reduces to 35 mm and the toe displacement decreases to 16 mm, with the total deformation reducing to 19 mm. This indicates that lowering the position of the surcharge load substantially reduces lateral deformation along the longer side of the excavation, thereby improving the overall stability of the system.

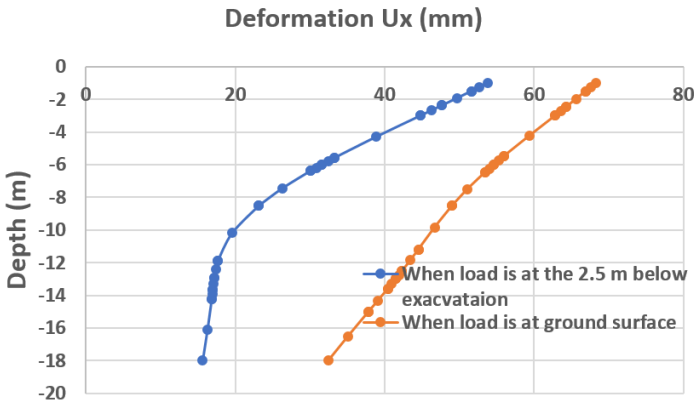


Figure 9. Ux effect of position of surcharge load, longer side of excavation

Table 8. Ux effect of position of surcharge load, longer side of excavation

| Loading Condition | Head Displacement (m) | Toe Displacement (-18m) | Total Delta (0m to -18m) |
|---|---|---|---|
| At Ground Surface | 67 mm | 32 mm | 35 mm |
| 2.5m Below Excavation | 35 mm | 16 mm | 19 mm |

The comparison of horizontal displacement ($u_x$) between the Mohr–Coulomb (MC) and Modified Cam Clay (MCC) models along the longer side of the excavation (corner pile condition) is presented in Figure 10 and summarized in Table 9. The MC model predicts a significantly higher peak displacement of 50 mm at a depth of approximately -10 m, with a toe displacement of 24 mm at −18 m. In contrast, the MCC model shows a much stiffer response, with a reduced peak displacement of 8 mm occurring at about −9 m depth and a toe displacement of only 2 mm. This comparison indicates that the MCC model provides a more restrained and realistic prediction of soil deformation under excavation loading, effectively capturing the stress–strain behavior of soft soils and resulting in substantially lower lateral movements compared to the MC model.

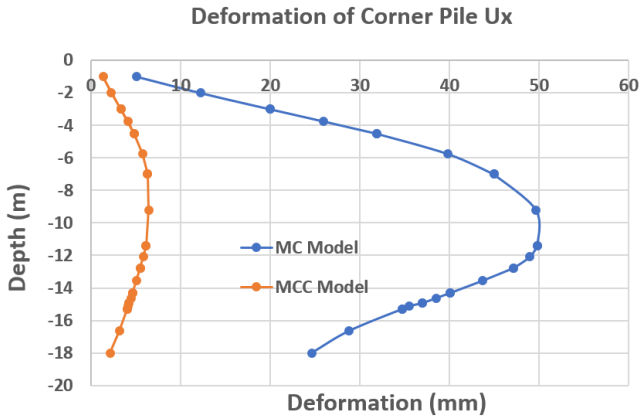


Figure 10. Ux comparison of two models, longer side of excavation, corner pile

Table 9. Ux comparison of two model, longer side of excavation, corner pile

| Model Type | Peak Displacement (mm) | Depth of Peak (m) | Toe Displacement (-18m) |
|---|---|---|---|
| MC Model | 50 mm | -10 m | 24 mm |
| MCC Model | 8 mm | -9 m | 2 mm |

The comparison of vertical displacement ($u_y$) between the Mohr–Coulomb (MC) and Modified Cam Clay (MCC) models along the longer side of the excavation (corner pile condition) is presented in Figure 11 and summarized in Table 10. The MC model predicts a higher deformation response, with a maximum positive deflection of 30 mm and a significant negative deflection of −26 mm occurring at the excavation head, while the peak positive displacement occurs at a depth of approximately −13.0 m. In contrast, the MCC model shows a more restrained response, with a maximum positive deflection of only 9 mm and no negative deflection, with the peak occurring

at around −9.5 m depth. This indicates that the MCC model captures a stiffer and more realistic soil response under excavation loading, resulting in substantially reduced vertical movements compared to the MC model.

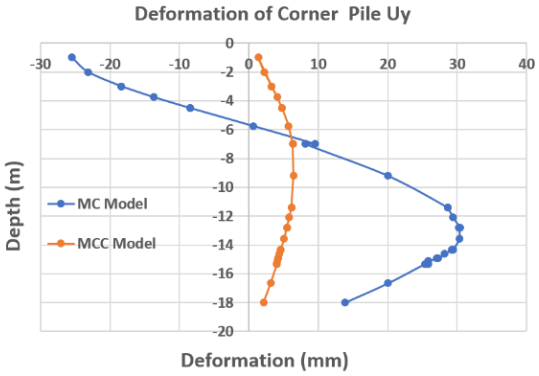


Figure 11. Uy Comparison of two model, longer side of excavation, corner pile

Table 10. Uy Comparison of two model, longer side of excavation, corner pile

| Model Type | Max Positive Deflection (mm) | Max Neg. Deflection (mm) | Depth of Positive Peak (m) |
|---|---|---|---|
| MC Model | 30 mm | -26 mm (at head) | -13.0 m |
| MCC Model | 9 mm | 0 mm | -9.5 m |

The comparison of horizontal displacement ($u_x$) of the capping beam between the Mohr–Coulomb (MC) and Modified Cam Clay (MCC) models along the longer side of the excavation is presented in Figure 12 and summarized in Table 11. The MC model predicts a significantly higher peak deformation of 200 mm occurring near −95.5 m length, with end displacements of −5 mm. In contrast, the MCC model shows a much stiffer response, with a reduced peak deformation of 18 mm occurring at approximately −94.0 m, and end displacements of −2 mm. This comparison clearly indicates that the MCC model provides a more restrained and realistic prediction of capping beam deformation, significantly reducing structural movements compared to the MC model and better capturing soil–structure interaction effects.

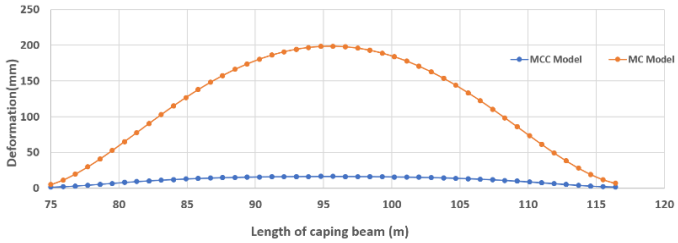


Figure 12. Ux comparison of two model, capping beam deformation, longer side of excavation

Table 11. Ux comparison of two model, capping beam deformation, longer side of excavation

| Model Type | Peak Deformation (mm) | Location of Peak (Length) (m) | Displacement at Ends (mm) |
|---|---|---|---|
| MC Model | 200 mm | -95.5 m | -5 mm |
| MCC Model | 18 mm | -94.0 m | -2 mm |

The effect of pile diameter on horizontal displacement ($u_x$) site along the longer side of the excavation is presented in Figure 13 and summarized in Table 12. The results indicate that increasing the pile diameter leads to a gradual reduction in lateral deformation. For a pile diameter of 0.65 m, the peak deformation is 15.0 mm at a depth of approximately −9.5 m. When the diameter is increased to 0.80 m, the peak deformation reduces to 13.5 mm at −8.5 m, corresponding to a 10% reduction. Further increasing the diameter to 0.90 m results in a peak deformation of 12.3 mm at −8.5 m, representing an overall reduction of 18% compared to the 0.65 m case. This demonstrates that larger pile diameters enhance system stiffness and effectively reduce lateral ground movements in excavation support systems.

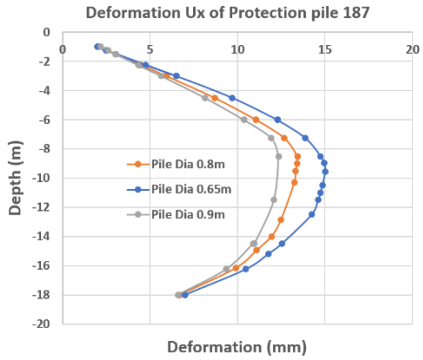


Figure 13. Ux effect on pile diameter, longer side of excavation

Table 12. Ux effect on pile diameter, longer side of excavation

| Pile Diameter (m) | Peak Deformation (mm) | Depth of Peak (m) | Reduction of Peak vs 0.65m |
|---|---|---|---|
| 0.65m | 15.0 mm | -9.5 m | Basis |
| 0.80m | 13.5 mm | -8.5 m | 10 % |
| 0.90m | 12.3 mm | -8.5 m | 18 % |

Figure 14 and Table 13 show that horizontal displacement ($u_x$) at 8.5 m depth along the longer side decreases with increasing pile diameter. Deformation reduces from 15.1 mm (0.65 m) to 13.4 mm (0.80 m) and 12.3 mm (0.90 m), indicating up to 18.5% improvement. This demonstrates that larger pile diameters increase stiffness and effectively control lateral ground movement. Although the 0.90 m diameter pile showed the minimum lateral deformation, the 0.80 m diameter pile also provided significant deformation reduction and may represent a practical balance between structural performance and construction economy.

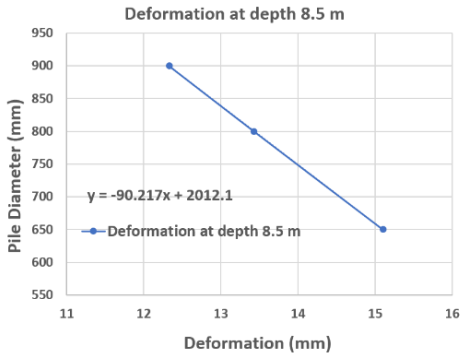


Figure 14. Ux effect on pile diameter at 8.5 m depth, longer side of excavation

Table 13. Ux effect on pile diameter at 8.5 m depth, longer side of excavation

| Pile Diameter (m) | Deformation (mm) | Efficiency Gain (Reduction) |
|---|---|---|
| 0.90 m | 12.3 mm | 18.5 % (vs. 0.65m) |
| 0.80 m | 13.4 mm | 11.2% (vs. 0.65m) |
| 0.65 m | 15.1 mm | Baseline |

The effect of pile diameter on surface settlement near the excavation area along the longer side of the site is presented in Figure 15 and summarized in Table 14. The results indicate a clear reduction in ground settlement with increasing pile diameter. For the baseline case of 0.65 m diameter piles, the peak surface settlement is 140 mm occurring at a distance of 73 m from the excavation. When the pile diameter is increased to 0.80 m, the peak settlement reduces to 108 mm at approximately 72 m, representing a 23% reduction. Further increasing the diameter to 0.90 m results in a minimum settlement of 92 mm at about 75 m, corresponding to a 34% reduction compared to the baseline case. This trend demonstrates that increasing pile diameter significantly enhances system stiffness and effectively mitigates surface settlement in the influence zone of deep excavations.

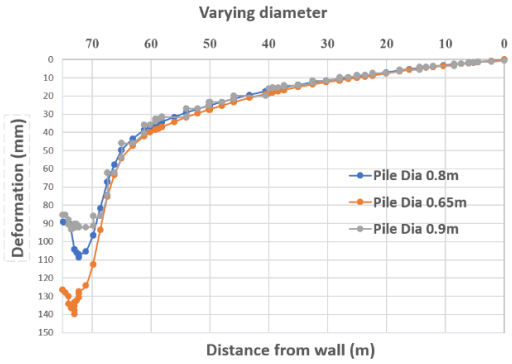


Figure 15. Ux effect on pile diameter near the excavation area (Surface Settlement (mm) vs Diameter (m); longer side of excavation

Table 14. Ux effect on pile diameter near the excavation area (Surface Settlement (mm) vs Diameter (m); longer side of excavation

| Pile Diameter (m) | Peak Settlement (mm) | Distance of Peak (m) | % Reduction vs. 0.65m |
|---|---|---|---|
| 0.65 m | 140 mm | 73 m | Baseline |
| 0.80 m | 108 mm | 72 m | 23% |
| 0.90 m | 92 mm | 75 m | 34% |

Figure 16 and Table 15 show that increasing pile diameter reduces peak capping beam deformation along the longer side, while the peak location remains at about 110 m. Deformation decreases from 82 mm (0.65 m) to 71 mm (0.80 m) and 73 mm (0.90 m), indicating up to 13% reduction. This confirms that larger pile diameters enhance stiffness and reduce beam deformation.

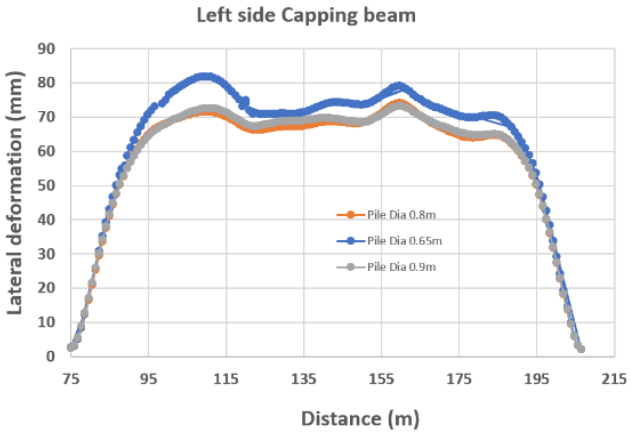


Figure 16. Effect on capping beam (Peak Lateral Deformation, longer side of excavation)

Table 15. Effect on capping beam (Peak Lateral Deformation, longer side of excavation)

| Pile Diameter (m) | Peak Deformation (mm) | Location of Peak (m) | % Reduction vs. 0.65m |
|---|---|---|---|
| 0.65 m | 82 mm | 110 m | Baseline |
| 0.90 m | 73 mm | 110 m | 11% |
| 0.80 m | 71 mm | 110 m | 13% |

The bending moment distribution in the 0.65 m diameter pile at the excavation site along the longer side of the excavation is presented in Figure 17. The results indicate that the maximum bending moment is primarily induced near the capping beam level due to lateral loading effects, with a peak moment of approximately 43 kN·m/m. This moment is transferred from the capping beam into the pile and gradually dissipates with depth, approaching zero at greater depths where the pile is laterally restrained by surrounding soil. This behavior reflects the typical flexural response of piles in deep excavation systems, where bending effects are concentrated in the upper active zone and diminish with increasing embedment depth due to soil confinement and increased passive resistance.

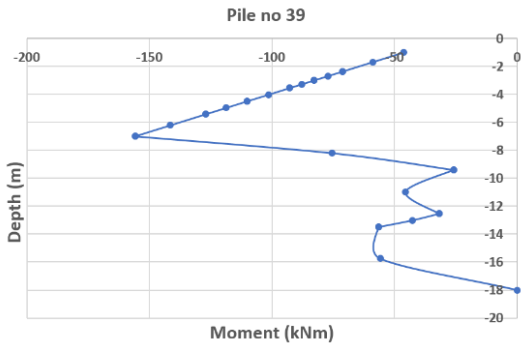


Figure 17. Bending moment of pile of 0.65m dia, longer side of excavation

## 4. Validation

The results obtained from the PLAXIS 3D modeling are validated against published literature, empirical methods, and relevant IS codes to ensure reliability and consistency. As part of this validation, p-y curves for the soft soil were generated using the Matlock (1970) empirical relationship, where soil resistance and corresponding pile deformation were computed at various excavation depths. The analysis indicates that while the overall trends remain consistent-providing confidence in the numerical modeling-there are observable differences in the peak pile displacements. Specifically, at an excavation depth of 8.5 m, the finite element model recorded relatively higher peak displacements of approximately 40 mm and 46 mm, as illustrated in Figure 18 and Figure 19. These variances are largely attributed to the fundamental differences in modeling approaches: whereas the Matlock formulation relies on discrete, independent Winkler springs, the 3D finite element analysis captures the complex SSI effect and the continuous nature of the soil mass. Despite the fact that the generated curves do not match the empirical values exactly, their consistent non-linear progression confirms an acceptable agreement between the theoretical predictions and the numerical results.

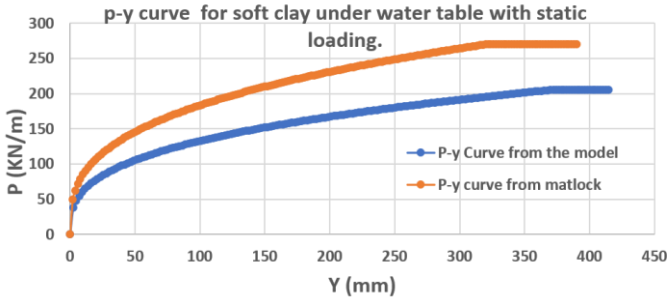


Figure 18. Comparison of PLAXIS 3D and Matlock (1970) p-y curves at an arbitrary pile depth of 17 m

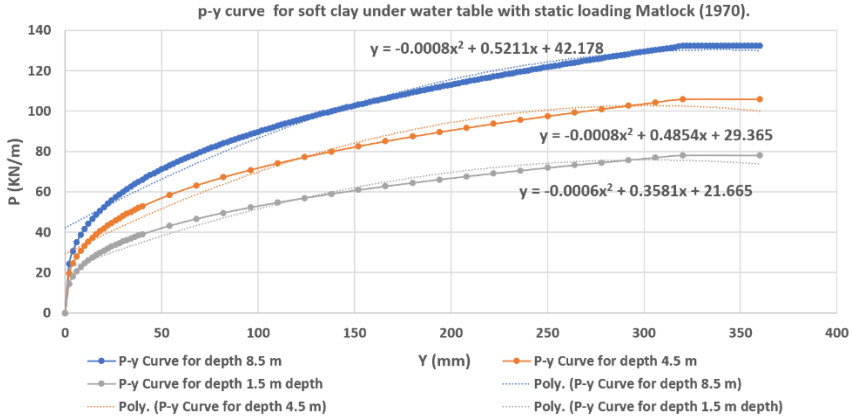


Figure 19. Comparison of PLAXIS 3D and Matlock (1970) p-y responses for soft clay at different excavation depths under static loading

Validation was performed using the Matlock (1970) p–y method and compared with PLAXIS 3D results (Figure 19). Both show similar non-linear trends, though PLAXIS predicts higher displacements due to its full soil–

structure interaction modeling compared to the simplified Winkler approach in Matlock. Validation is therefore based on trend agreement rather than exact numerical match. The numerical results are consistent with previous studies on deep excavations in soft clay (Peck, 1969; Clough and O'Rourke, 1990; Sharma et al., 2019), supporting the adopted methodology. Future studies should include field data for further validation.

## 5. Conclusion

The finite element analysis of the Ramshahapath excavation site reveals that the SSI effect creates a critical influence zone extending approximately 10m from the excavation, where surface settlements exceed 40mm and threaten the stability of adjacent structures. The study demonstrates that surface loading increases retaining structure deformation by 52.11% compared to subsurface loading, though applying a surcharge at a depth of 2.5 m effectively mitigates this, reducing displacements to Ux = 5.9mm and Uy = 5.01mm. A significant disparity was observed between constitutive models: the Mohr–Coulomb (MC) model over-predicted deformations at Ux = 49.8mm, whereas the Modified Cam Clay (MCC) model provided more realistic estimates (Ux = 6.67mm, Uy = 6.13mm), proving its superior suitability for these soft soil conditions. Furthermore, structural stiffness plays a vital role, as reducing pile diameter from 0.9 m to 0.65 m increased deformation by 18.4%. These findings suggest that future geotechnical assessments must move beyond the MC model in favor of advanced constitutive models like MCC, while incorporating field monitoring, irregular excavation geometries, and comparative multi-platform numerical analyses to ensure the robustness of support system designs.

## Acknowledgements

The authors sincerely thank the concerned authorities for granting access to undisturbed soil samples, providing field measurements, and offering valuable support that was essential for the successful completion of this study.

## References

ASTM D2435 / D2435M-11. 2020. Standard Test Methods for One-Dimensional Consolidation Properties of Soils Using Incremental Loading. *ASTM International*, West Conshohocken, PA.

Brinkgreve, R. B. J., Kumarswamy, S., & Swolfs, W. M. 2023. *PLAXIS 3D Reference Manual*. Bentley Systems, Inc.

Bowles, J.E., 1988. *Foundation analysis and design*. 4th ed. New York: McGraw-Hill Book Company.

Chang, M., 2000. Basal stability analysis of braced cuts. *Journal of Geotechnical and Geoenvironmental Engineering*, 126(3), pp.276–279.

Clough, G.W. and O'Rourke, T.D., 1990. Construction induced movements of in-situ walls. In: *Design and performance of earth retaining structures*. ASCE Special Conference, Ithaca, New York, pp.439–470.

Clough, G.W., Smith, E.W. and Sweeney, B.P., 1989. Movement of excavation support system by iterative method. In: *Foundation Engineering: Current Principles and Practices*, Vol. 2. New York: ASCE.

Clough, G.W. and O'Rourke, T.D., 1990. Construction induced movements of insitu walls. In: *Proceedings of the Conference on Design and Performance of Earth Retaining Structures*. Ithaca, NY: ASCE, pp.439–470.

Goh, A.I., 1990. Assessment of basal stability for braced excavation systems using the finite element method. *Computers and Geotechnics*, 10(4), pp.325–338.

Kulhawy, F.H., 1992. On evaluation of static soil properties. In: Seed, R.B. and Boulanger, R.W., eds. *Proceedings of the H. Bolton Seed Memorial Symposium, Vol. 2: Laboratory Shear Strength of Soil. Berkeley*, California: American Society of Civil Engineers, pp.95–115.

Mana, A.I. and Clough, G.W., 1981. Prediction of movements for braced cuts in clay. *Journal of the Geotechnical Engineering Division*, 107(6), pp.759–777.

Peck, R.B., 1969. Deep excavations and tunneling in soft ground. In: *Proceedings of the 7th International Conference on Soil Mechanics and Foundation Engineering*. Mexico City, State-of-the-Art Volume, pp.225–290.

Matlock, H., 1970. Correlation for design of laterally loaded piles in soft clays. In: *Offshore Technology Conference. Houston*, Texas, pp.577–594.

Nagaraj, T.S. and M.B., 1985. Prediction of the preconsolidation pressure and recompression index of soils. *Geotechnical Testing Journal (ASTM)*, pp.199–202.

O'Rourke, T.A., 1990. Design and performance of earth retaining structures. *Geotechnical Special Publication No. 25*. American Society of Civil Engineers, pp.22–51.

Reese, L.C., 1974. Analysis of laterally loaded piles in sand. In: *Proceedings of the 6th Offshore Technology Conference*, Vol. 2. Houston, TX, pp.272–283.

Roscoe, K. H., & Burland, J. B. 1968. On the generalized stress-strain behaviour of 'wet' clay. *Engineering Plasticity*, Cambridge University Press, pp.535–609.

Sharma, S., Deng, J., & Zhao, M. 2019. Numerical modeling of the performance of deep excavations in soft clay. *Underground Space*, 4(2), pp.115–130.

Skempton, A. W. 1944. Notes on the compressibility of clays. *Quarterly Journal of the Geological Society*, 100(1-4), pp.119–135.

Terzaghi, K., 1943. *Theoretical soil mechanics*. New York: John Wiley.

Terzaghi, K., Peck, R. B., & Mesri, G. 1996. *Soil Mechanics in Engineering Practice (3rd ed.)*. John Wiley & Sons, New York.

Wong, K.S., Goh, A.T.C., Jaritngam, S. and Chang, I.J.D., 1998. Optimization of jet grout configuration for braced excavation in soft clay. In: *Proceedings of the 2nd Conference on Ground Improvement Techniques. Singapore*.